Semarak Engineering Journal

Journal homepage:
https://semarakilmu.my/index.php/sej/index
ISSN: 3036-0145



Impact of Mass Flow Rates and Air Channel Height on Solar Air Heater Performance with Rectangular Encapsulated Absorbent Surface

Rana mohammed shakir[1,*], Ali Lafta Ekaid[1], Hasanen Mohammed Hussein[1]

[1] Mechanical Engineering Department, University of Technology, Baghdad, Iraq

ARTICLE INFO

Article history:
Received 12 July 2026
Received in revised form 30 September 2026
Accepted 2 November 2026
Available online 24 November 2026

Keywords:
solar air heater; mass flow rate; air channel height; solar energy; Heat transfer; sustainable energy

ABSTRACT

This study examines the effect of mass flow rates and air channel height on the solar air heater performance. In order to get an accurate assessment of the solar collector's performance, the Pressure-Linked Equations utilized the Semi-Implicit method (SIMPLE) approach in FORTRAN. Data was collected by adjusting the air flow rates and airflow channel heights, and analyzing the outlet temperature, convective heat transfer, Nusselt number, and heat transfer efficiency. The results suggest that increasing the air flow rates typically increase the convective heat transfer and decrease the out-air temperature. also, the air channel height has varying effects on thermal stratification and overall efficiency. These findings indicate that by adjusting operating parameters such as mass flow rates and air channel height enhance the heat transfer efficiency in solar heating applications This study offers useful information that may be used to develop and deploy solar thermal systems with high efficiency.

1. Introduction

The increasing demand for renewable and sustainable energy sources has encouraged researchers and engineers to explore various approaches to enhancing the heat transfer performance of solar air heater (SAH) systems. SAHs have attracted considerable attention owing to their simple design, cost-effectiveness, and potential applications in space heating and agricultural drying [1]. Despite their numerous advantages [2], maximizing their thermal performance remains a significant challenge. Among the various operating and geometrical parameters, air mass flow rate and air channel height play crucial roles in determining the thermal efficiency and overall performance of these systems.

Hussam Dheyab *et al.* [3] investigated the optimal air gap height in a solar air heating system. Four solar air heaters with different air channel heights of 3, 5, 7, and 9 cm were experimentally evaluated. The findings revealed that the channel height of 3 cm consistently produced the highest outlet air temperature throughout the experimental period, highlighting the importance of optimizing channel geometry to improve thermal performance.

* *Corresponding author.*
E-mail address: ranaalassadi.211@gmail.com

https://doi.org/10.37934/sej.17.1.164183

Zainab Saberi *et al.* [4] investigated a solar air heater incorporating 210 aluminum rods, each with a height of 0.02 m, attached to the absorber surface to increase the effective heat transfer area. Additionally, fin structures were incorporated to enhance heat transfer from the absorber surface to the flowing air. The results demonstrated that the heat transfer efficiency ranged from 57.2% to 77.4%, indicating the potential of extended surfaces to improve the thermal performance of SAHs.

Daoud Halassa *et al.* [5] investigated the optimal configuration of flat-plate solar air heaters equipped with single-pass and double-pass collectors. The authors also examined the influence of geometrical parameters on temperature uniformity within a naturally ventilated indirect solar dryer. Computational fluid dynamics (CFD) simulations revealed that the single-pass solar collector provided a more uniform temperature distribution than the double-pass configuration.

Arunkumar Sheshadri *et al.* [6] conducted a numerical investigation to enhance the thermal performance of a flat-plate solar air heater by incorporating chamfered turbulators beneath the absorber plate. The results indicated that a turbulator with a diameter of 7 mm and a chamfer angle of 30° significantly enhanced flow turbulence, yielding a thermal enhancement factor of 1.15 across the investigated flow range. Similarly, Khudheyer Mushatet *et al.* [7] investigated the thermal performance of a solar air heating system equipped with rectangular ribs of different heights (1, 2, and 3 cm) to introduce artificial roughness on the absorber surface. The findings demonstrated that incorporating ribs with a height of 3 cm increased thermal efficiency by 11.981%. Collectively, these studies demonstrated the effectiveness of artificial roughness and turbulence-promoting structures in enhancing convective heat transfer within solar air heaters.

Yussra Abdullah *et al.* [8] employed CFD simulations to investigate the physical and operating characteristics of a solar air heating system. The results indicated that variations in the airflow parameters influenced the outlet air temperature, emphasizing the importance of optimizing airflow conditions to enhance thermal performance.

In addition to geometrical modifications and airflow optimization, thermal energy storage has been investigated as an alternative approach to improving the performance of solar heating systems. Maithum Hussein Rasheed [9] investigated the optimal water proportion and the most suitable phase change material (PCM) for enhancing thermal energy storage efficiency. The study aimed to develop a solar heating system capable of maximizing thermal energy storage during daylight hours for subsequent heating applications under specific local climatic conditions.

Mayank Srivastava *et al.* [10] investigated the influence of different absorber materials, including rocks, wire mesh, strips, and wood-based materials, on the thermal performance of solar air heaters. The study aimed to identify the absorber material that provided the highest operating temperature and thermal efficiency, highlighting the importance of material selection in solar air heater design.

Le Minh Nhut *et al.* [11] employed analytical modeling and multi-objective optimization to evaluate the exergy and effective efficiencies of a multi-pass solar air collector equipped with fins. The investigation considered several design and operating parameters, including airflow rate, collector height, collector length, and fin pitch diameter. The optimization process was performed based on three primary performance criteria: thermal efficiency, effective efficiency, and exergy efficiency. This approach provided a comprehensive framework for evaluating solar air collector performance beyond conventional thermal efficiency assessments.

Muhammad Harun *et al.* [12] examined the influence of various geometrical and material parameters, including absorber surface material, glazing thickness, air channel height, and absorber plate thickness, on the thermal efficiency of solar collectors. The investigation emphasized the importance of appropriately selecting construction materials and geometrical configurations to improve collector performance.

Abdulwahhab Hardan *et al.* [13] investigated the thermal performance of a solar collector incorporating an evacuated-tube heat pipe system. Longitudinal copper fins were attached to the heat pipes to enhance heat transfer and improve thermal efficiency. The findings revealed that the finned evacuated-tube configuration exhibited superior thermal efficiency compared with the conventional evacuated-tube configuration, further demonstrating the effectiveness of extended heat transfer surfaces in solar thermal applications.

Overall, previous investigations demonstrated that the thermal performance of solar air heaters was strongly influenced by geometrical configurations, absorber materials, airflow characteristics, turbulence-promoting structures, and thermal energy storage mechanisms. Although considerable attention was devoted to enhancing heat transfer through structural modifications and material optimization, the combined influence of air mass flow rate and air channel height warrants further investigation. A systematic evaluation of these parameters would provide a better understanding of their interactions and facilitate the development of more efficient solar air heating systems.

2. Methodology

2.1 Problem Description

The present study investigated the thermal performance of a solar air heater under specified operating conditions, including an ambient temperature of 20 °C, a wind speed of 1.5 m/s, a solar heat flux of approximately 502 W/m², and four different air mass flow rates of 0.01, 0.02, 0.03, and 0.04 kg/s. Additionally, a numerical investigation was conducted to evaluate the influence of air channel height on the thermal performance of the solar air heater. Four different air channel heights of 2, 4, 6, and 8 cm were investigated at two air mass flow rates of 0.01 and 0.04 kg/s to assess the effects of channel geometry and airflow conditions on heat transfer performance.

The solar air heater had overall dimensions of 2.3 m × 0.34 m, with a test section measuring 1.3 m × 0.3 m. Plywood with a thickness of 0.02 m was used as an insulating material. The inlet section was designed with a length of 0.6 m to facilitate the development of fully developed airflow before entering the test section, while the outlet section had a length of 0.4 m. The width-to-height ratio (W/H) of the air passage was maintained at approximately 7 for the baseline configuration, in accordance with the recommendations of the American Society of Heating, Refrigerating and Air-Conditioning Engineers (ASHRAE) [14].

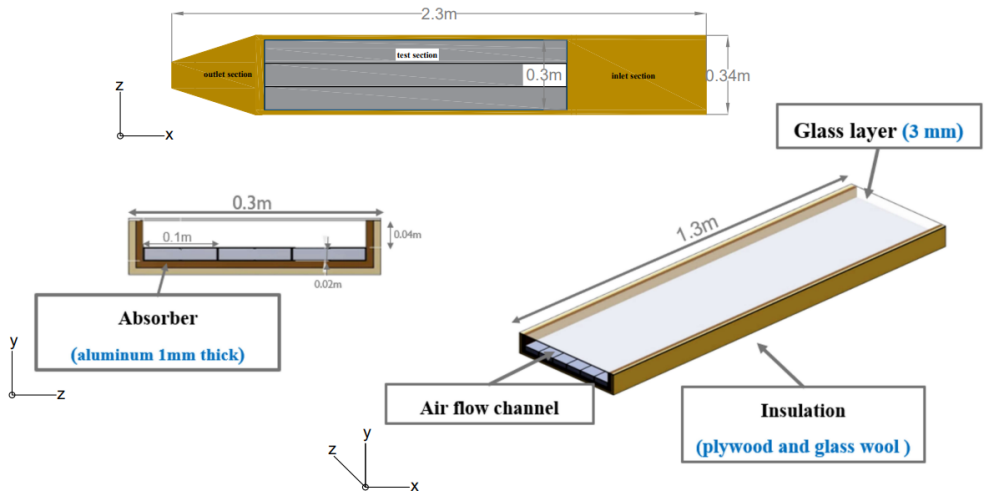


Fig. 1. geometry of solar heating system

Table 1
Specifications SAH materials

PARAMETER	VALUES
Thickness of glass	4mm
Transmittance of glass	0.87
Glass emissivity	0.9
Aluminum thickness	1mm
Aluminum absorbance	0.1
Opaque black paint	0.9

To formulate and solve the governing equations describing the thermal and fluid flow characteristics of the solar air heater, the following assumptions were adopted in the mathematical model:

- The airflow was assumed to be three-dimensional, turbulent, and incompressible.
- Heat transfer within the air channel was dominated by forced convection.
- The inlet air temperature was assumed to be equal to the ambient air temperature.
- The thermophysical properties of air were assumed to remain constant, irrespective of temperature variations.
- Heat losses through the bottom and sidewalls of the solar collector were neglected owing to adequate thermal insulation.
- The computational domain was assumed to be symmetrical in the z-direction.
- The investigation was conducted using the average solar radiation intensity during peak sunshine hours.

2.2 Governing Equations

A numerical mathematical model based on the finite volume method (FVM) was developed and implemented in FORTRAN. The Semi-Implicit Method for Pressure-Linked Equations (SIMPLE) algorithm was employed to establish pressure–velocity coupling [15]. The governing Navier–Stokes equations were discretized using the finite volume method to characterize the fluid flow and heat transfer mechanisms within the solar air heater. Furthermore, energy balance equations were employed to describe the heat transfer processes associated with the glass cover and absorber plate.

The governing equations consisted of the conservation equations for mass, momentum, and thermal energy, together with the transport equations for turbulent kinetic energy and its dissipation rate. The following partial differential equations were solved within the air channel [16]. For clarity, the material derivative is denoted by D/Dt = ∂/∂t + u∂/∂x + v∂/∂y + w∂/∂z.

Continuity equation:

$$\frac{\partial \rho}{\partial t} + \frac{\partial (\rho u)}{\partial x} + \frac{\partial (\rho v)}{\partial y} + \frac{\partial (\rho w)}{\partial z} = 0 \quad (1)$$

Momentum equation in the x-direction (u-momentum):

$$\begin{aligned} \rho \frac{Du}{Dt} = \quad & -\frac{\partial p}{\partial x} + \frac{\partial}{\partial x}\left[(\mu + \mu_t)\left(2\frac{\partial u}{\partial x}\right)\right] \\ & + \frac{\partial}{\partial y}\left[(\mu + \mu_t)\left(\frac{\partial u}{\partial y} + \frac{\partial v}{\partial x}\right)\right] \\ & + \frac{\partial}{\partial z}\left[(\mu + \mu_t)\left(\frac{\partial u}{\partial z} + \frac{\partial w}{\partial x}\right)\right] \end{aligned} \quad (2)$$

Momentum equation in the y-direction (v-momentum):

$$\rho\frac{Dv}{Dt} = -\frac{\partial p}{\partial y} + \frac{\partial}{\partial x}\left[(\mu+\mu_t)\left(\frac{\partial v}{\partial x}+\frac{\partial u}{\partial y}\right)\right] + \frac{\partial}{\partial y}\left[(\mu+\mu_t)\left(2\frac{\partial v}{\partial y}\right)\right] + \frac{\partial}{\partial z}\left[(\mu+\mu_t)\left(\frac{\partial v}{\partial z}+\frac{\partial w}{\partial y}\right)\right] \quad (3)$$

Momentum equation in the z-direction (w-momentum):

$$\rho\frac{Dw}{Dt} = -\frac{\partial p}{\partial z} + \frac{\partial}{\partial x}\left[(\mu+\mu_t)\left(\frac{\partial w}{\partial x}+\frac{\partial u}{\partial z}\right)\right] + \frac{\partial}{\partial y}\left[(\mu+\mu_t)\left(\frac{\partial w}{\partial y}+\frac{\partial v}{\partial z}\right)\right] + \frac{\partial}{\partial z}\left[(\mu+\mu_t)\left(2\frac{\partial w}{\partial z}\right)\right] \quad (4)$$

Thermal energy equation:

$$\rho\frac{DT}{Dt} = \frac{\partial}{\partial x}\left[\left(\frac{\mu}{Pr}+\frac{\mu_t}{\sigma_T}\right)\frac{\partial T}{\partial x}\right] + \frac{\partial}{\partial y}\left[\left(\frac{\mu}{Pr}+\frac{\mu_t}{\sigma_T}\right)\frac{\partial T}{\partial y}\right] + \frac{\partial}{\partial z}\left[\left(\frac{\mu}{Pr}+\frac{\mu_t}{\sigma_T}\right)\frac{\partial T}{\partial z}\right] \quad (5)$$

Turbulent kinetic energy equation:

$$\rho\frac{Dk}{Dt} = \frac{\partial}{\partial x}\left[\left(\mu+\frac{\mu_t}{\sigma_k}\right)\frac{\partial k}{\partial x}\right] + \frac{\partial}{\partial y}\left[\left(\mu+\frac{\mu_t}{\sigma_k}\right)\frac{\partial k}{\partial y}\right] + \frac{\partial}{\partial z}\left[\left(\mu+\frac{\mu_t}{\sigma_k}\right)\frac{\partial k}{\partial z}\right] + P_k + G_k - \rho\varepsilon + D \quad (6)$$

Turbulent kinetic energy dissipation rate equation:

$$\rho\frac{D\varepsilon}{Dt} = \frac{\partial}{\partial x}\left[\left(\mu+\frac{\mu_t}{\sigma_\varepsilon}\right)\frac{\partial \varepsilon}{\partial x}\right] + \frac{\partial}{\partial y}\left[\left(\mu+\frac{\mu_t}{\sigma_\varepsilon}\right)\frac{\partial \varepsilon}{\partial y}\right] + \frac{\partial}{\partial z}\left[\left(\mu+\frac{\mu_t}{\sigma_\varepsilon}\right)\frac{\partial \varepsilon}{\partial z}\right] + C_{\varepsilon 1}f_1(P_k + C_{\varepsilon 3}G_k)\frac{\varepsilon}{k} - \rho C_{\varepsilon 2}f_2\frac{\varepsilon^2}{k} + E \quad (7)$$

The production of turbulent kinetic energy due to mean velocity gradients was expressed as

$$P_k = \mu_t\left[\, 2\left(\frac{\partial u}{\partial x}\right)^2 + 2\left(\frac{\partial v}{\partial y}\right)^2 + 2\left(\frac{\partial w}{\partial z}\right)^2 + \left(\frac{\partial u}{\partial y}+\frac{\partial v}{\partial x}\right)^2 + \left(\frac{\partial v}{\partial z}+\frac{\partial w}{\partial y}\right)^2 + \left(\frac{\partial w}{\partial x}+\frac{\partial u}{\partial z}\right)^2\right] \quad (8)$$

The buoyancy-induced production of turbulent kinetic energy was defined as

$$G_k = -\frac{\mu_t}{\sigma_T}g\beta\frac{\partial T}{\partial y} \quad (9)$$

The turbulent dynamic viscosity was calculated using

$$\mu_t = \rho C_\mu f_\mu \frac{k^2}{\varepsilon} \tag{10}$$

The additional near-wall correction term in the turbulent kinetic energy equation was expressed as

$$D = -2\mu \left[\left(\frac{\partial \sqrt{k}}{\partial x}\right)^2 + \left(\frac{\partial \sqrt{k}}{\partial y}\right)^2 + \left(\frac{\partial \sqrt{k}}{\partial z}\right)^2 \right] \tag{11}$$

The additional correction term in the dissipation rate equation was expressed in compact tensor notation as

$$E = \frac{\mu \mu_t}{\rho} \sum_{i=1}^{3} \sum_{j=1}^{3} \sum_{l=1}^{3} \left(\frac{\partial^2 u_i}{\partial x_j \, \partial x_l} \right)^2 \tag{12}$$

Here, ρ is the air density; u, v, and w are the velocity components in the x-, y-, and z-directions, respectively; p is the pressure variable; T is the air temperature; μ is the molecular dynamic viscosity; μ_t is the turbulent dynamic viscosity; k is the turbulent kinetic energy; and ε is its dissipation rate. Pr represents the molecular Prandtl number, while σ_t, σ_k, and σε represent the turbulent diffusion parameters associated with thermal energy, turbulent kinetic energy, and its dissipation rate, respectively. The parameters fμ, f_1, and f_2 represent empirical correction functions associated with the low-Reynolds-number turbulence model.

The empirical constants employed in the low-Reynolds-number k–ε turbulence model originally proposed by Jones and Launder in 1972 [17] are presented in Table 2.

Table 2
k-ε model empirical constant by jones and launder in 1972

C_μ	$C_{\varepsilon 1}$	$C_{\varepsilon 2}$	σ_T	σ_K	σ_ε	f_1	f_2	f_μ
0.09	1.44	1.92	0.9	1	1.3	1.0	$-0.3exp(-Re_t^2)$	$exp\left(\frac{-2.5}{1+\frac{Re_t}{50}}\right)$

2.3 Boundary Conditions

The ambient temperature of the solar air heater (SAH) system was assumed to be 20 °C. The initial temperature estimates for the glass cover and absorber plate in the iterative numerical solution were set equal to the ambient temperature, as expressed below:

$$T_g = T_{up} = T_{amb} = 20\,°C$$

where T_g, T_{up}, and T_{amb} represent the temperatures of the glass cover, absorber plate, and ambient air, respectively.

A three-dimensional steady-state numerical approach was employed to simulate heat transfer through the solid components of the solar air heating system. The primary objective of the thermal simulation was to evaluate the various parameters influencing the thermal performance of the system under different operating conditions. To provide a comprehensive understanding of the heat transfer mechanisms, a thermal resistance network was employed to represent the conduction, convection, and radiation heat transfer processes within the solar air collector, as illustrated in Figure 2 [18]. The mathematical formulation was based on the principle of energy conservation, whereby

the net energy transfer to each component was zero under steady-state conditions, accounting for the absorbed solar radiation and the associated heat transfer mechanisms [19].

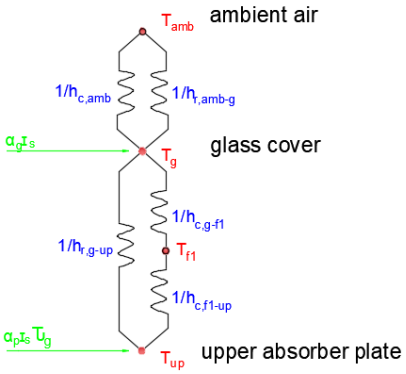


Fig. 2. Energy balance through the collector

Glass Cover

A fraction of the incident solar radiation was absorbed by the glass cover and converted into thermal energy. In addition, radiative heat exchange occurred between the glass cover and the absorber plate owing to the temperature difference between these two surfaces. The glass cover also exchanged heat with the ambient air through convection, with the sky through radiation, and with the airflow within the air channel through convection. The energy balance equation for the glass cover was expressed as follows:

$$\begin{aligned}\rho_g C_{p,g} V_g \frac{dT_g}{dt} = \quad & \alpha_g I A_g - h_{c,amb} A_g \left(T_g - T_{amb}\right) \\ & - h_{r,sky-g} A_g \left(T_g - T_{sky}\right) \\ & - h_{r,g-abs} A_g \left(T_g - T_{abs}\right) \\ & - h_{c,g-f} A_g \left(T_g - T_f\right) + k_g \delta_g A_g \frac{\partial^2 T_g}{\partial x^2}\end{aligned} \tag{13}$$

The convective heat transfer coefficient between the glass cover and the ambient air was determined as a function of wind velocity using the following correlations:

$$h_{c,amb} = h_{wind} = \begin{cases} 2.8 + 3.3 v_{wind}, & v_{wind} \leq 5 \text{ m/s} \\ 5.67 + 3.86 v_{wind}, & v_{wind} > 5 \text{ m/s} \end{cases}$$

The radiative heat transfer coefficient between the glass cover and the sky was calculated as

$$h_{r,sky-g} = \sigma \varepsilon_g \left(T_g^2 + T_{sky}^2\right)\left(T_g + T_{sky}\right)$$

The effective sky temperature was estimated using the following empirical correlation:

$$T_{sky} = 0.0552 T_{amb}^{1.5}$$

All absolute temperatures used in the radiation equations were expressed in Kelvin.

The radiative heat transfer coefficient between the glass cover and the absorber plate was determined as

$$h_{r,g-abs} = \frac{\sigma\left(T_g^2 + T_{abs}^2\right)\left(T_g + T_{abs}\right)}{1/\varepsilon_g + 1/\varepsilon_{abs} - 1}$$

The convective heat transfer coefficient between the glass cover and the flowing air was calculated as

$$h_{c,g-f} = \frac{q''_{g-f}}{T_g - T_b}$$

where q''_{g-f} represents the local convective heat flux from the glass cover to the airflow.

For a three-dimensional airflow channel, the bulk air temperature was determined using the mass-flow-weighted average temperature across the channel cross-section:

$$T_b = \frac{\int_{A_c} \rho u T \, dA}{\int_{A_c} \rho u \, dA}$$

where A_c represents the cross-sectional area of the air channel.

Top Absorber Plate

After passing through the transparent glass cover, a fraction of the incident solar radiation was absorbed by the absorber plate and converted into thermal energy. A portion of the absorbed thermal energy was subsequently transferred to the air flowing through the channel by forced convection [20]. Radiative heat exchange also occurred between the absorber plate and the glass cover.

Figure 2 illustrates the thermal energy balance associated with the absorber surfaces. The energy balance equation for the top absorber plate was expressed as follows:

$$\begin{aligned} \rho_{abs} C_{p,abs} V_{abs} \frac{dT_{abs}}{dt} = \quad & \alpha_{abs} \tau_g I A_{abs} \\ & - h_{r,g-abs} A_{abs} \left(T_{abs} - T_g\right) \\ & - h_{c,abs-f} A_{abs} \left(T_{abs} - T_f\right) \end{aligned} \tag{14}$$

The radiative heat transfer coefficient between the absorber plate and the glass cover was calculated as

$$h_{r,g-abs} = \frac{\sigma\left(T_g^2 + T_{abs}^2\right)\left(T_g + T_{abs}\right)}{1/\varepsilon_g + 1/\varepsilon_{abs} - 1}$$

The convective heat transfer coefficient between the absorber plate and the airflow was determined as

$$h_{c,abs-f} = \frac{q''_{abs-f}}{T_{abs} - T_b}$$

where q''_{abs-f} represents the local convective heat flux from the absorber plate to the airflow.

Inlet Boundary Conditions

Uniform velocity and temperature profiles were prescribed at the inlet of the solar air heater. The airflow was assumed to enter the channel in the axial direction, while the transverse velocity components were set to zero. The inlet air temperature was assumed to be equal to the ambient temperature.

The inlet boundary conditions were expressed as

$$\left.\begin{array}{ll} u(x,y,z) & = u_{in} \\ v(x,y,z) & = 0 \\ w(x,y,z) & = 0 \\ T(x,y,z) & = T_{in} \end{array}\right\} \quad \begin{array}{rl} x & = 0 \\ 0 < y & < h_{ch} \\ 0 < z & < W \end{array} \tag{15}$$

where u_{in} represents the inlet air velocity, T_{in} represents the inlet air temperature, h_{ch} denotes the air channel height, and W represents the channel width.

Outlet Boundary Conditions

At the outlet of the air channel, zero-gradient boundary conditions were imposed on the velocity components and temperature in the direction normal to the outlet plane. These conditions allowed the airflow to leave the computational domain without prescribing the outlet velocity and temperature profiles.

The outlet boundary conditions were expressed as

$$\frac{\partial \phi}{\partial x} = 0 \quad \begin{array}{rl} x & = L \\ 0 < y & < h_{ch} \\ 0 < z & < W \end{array} \tag{16}$$

where ϕ represents the dependent variables u, v, w, and T, while L denotes the total length of the computational domain.

Grid Independence Study

A grid independence study was conducted to evaluate the influence of grid resolution on the numerical predictions and to establish an appropriate computational grid for subsequent simulations. The computational domain of the air channel was discretized using four different grid resolutions of 200 × 60 × 20, 200 × 60 × 30, 200 × 60 × 40, and 200 × 60 × 50 nodes along the x-, z-, and y-directions, respectively.

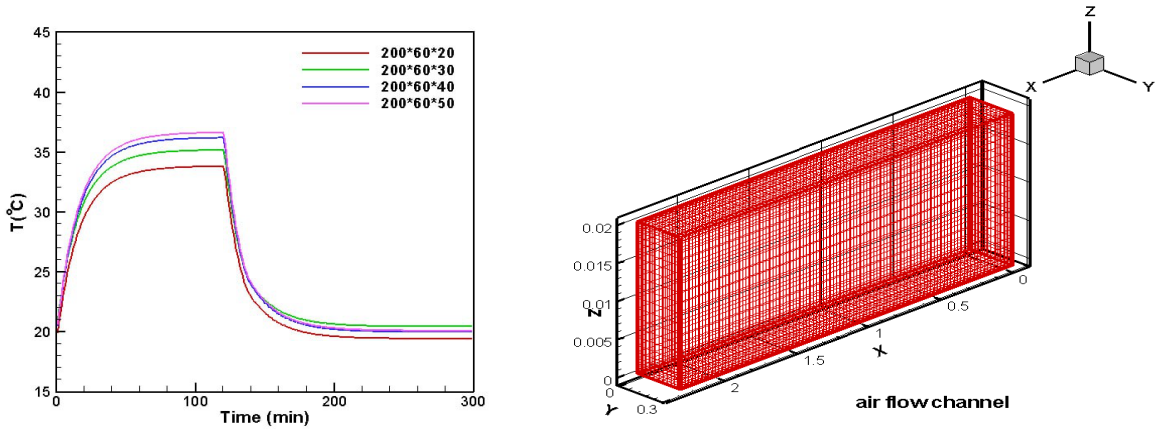


Fig. 3. (left)Grid independence test and (right) air channel Mesh of the computational domain

3. Results

The numerical model of the single-pass solar air heater (SAH) was evaluated by comparing the predicted outlet air temperatures with experimentally measured values under identical operating conditions, as shown in Figure 4. Comparisons were performed at air mass flow rates of 0.01, 0.02, and 0.03 kg/s. The comparison was reported to indicate satisfactory agreement between the numerical and experimental results, although the maximum deviation was not quantified in the supplied text.

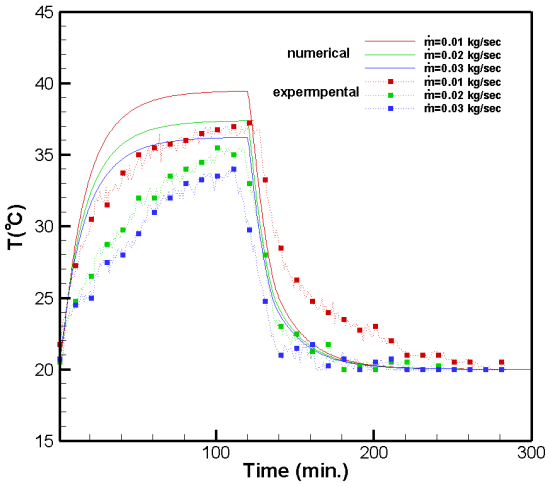


Fig. 4. Comparison of numerical and experimental outlet air temperatures under identical operating conditions

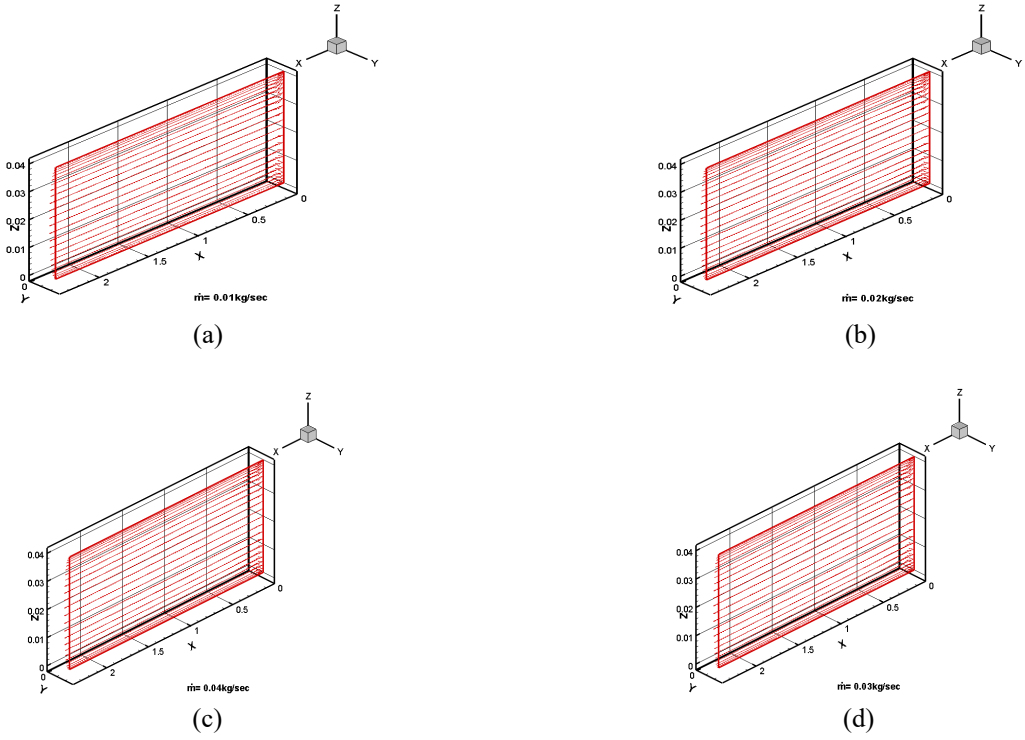
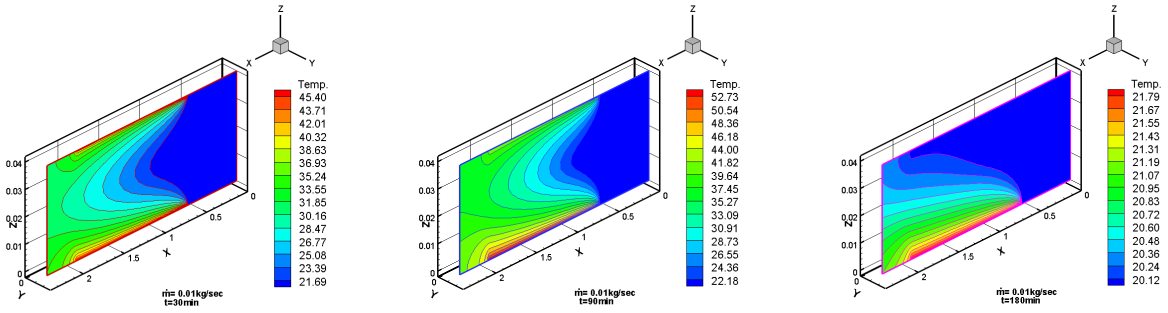


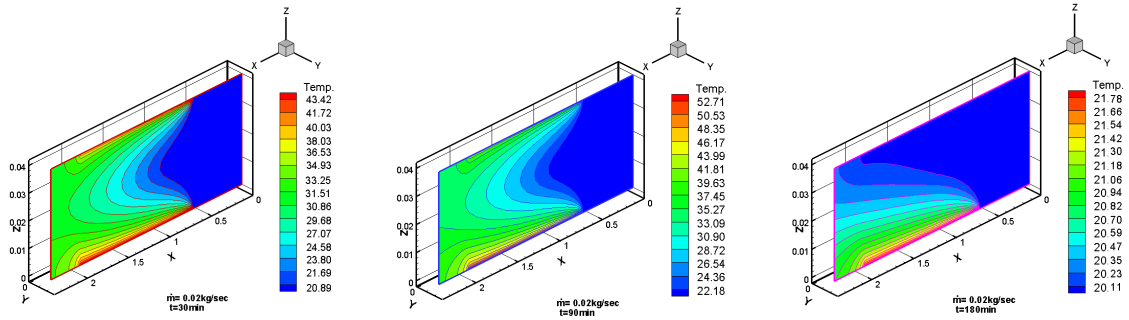
Fig. 5. Velocity vectors within the SAH at air mass flow rates of (a) 0.01, (b) 0.02, (c) 0.03, and (d) 0.04 kg/s under a solar irradiance of 502 W/m²

The temperature contours of the airflow, glass cover, and absorber plate provided insight into the spatial temperature distribution and heat transfer characteristics of the SAH. Figures 6–9 illustrate the air temperature distributions at elapsed times of 30, 90, and 180 min during the reported charging and discharging process for air mass flow rates of 0.01, 0.02, 0.03, and 0.04 kg/s. Downstream of the entrance region, heat was transferred from the absorber surface to the flowing air owing to the temperature difference between them.



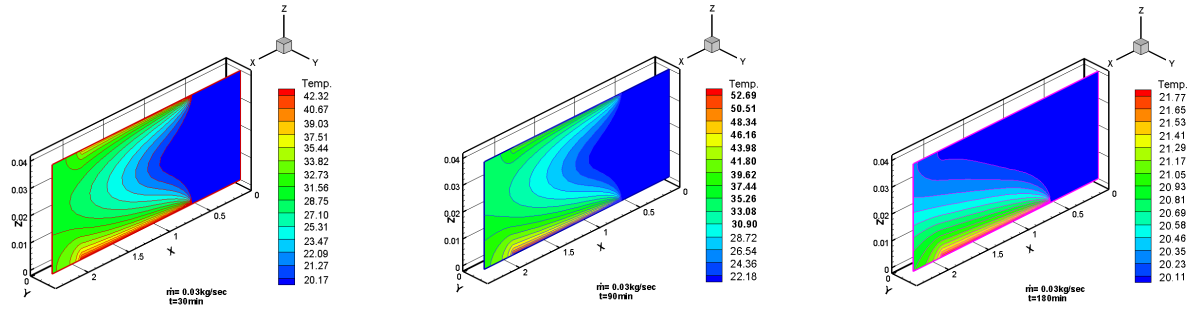
(a) (b) (c)

Fig. 6. Air temperature contours along the SAH channel at a mass flow rate of 0.01 kg/s: (a) 30 min, (b) 90 min, and (c) 180 min



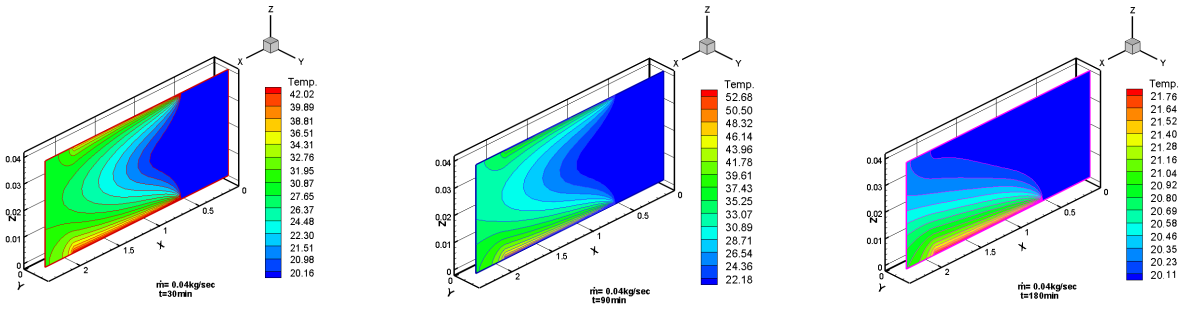
(a) (b) (c)

Fig. 7. Air temperature contours along the SAH channel at a mass flow rate of 0.02 kg/s: (a) 30 min, (b) 90 min, and (c) 180 min



(a) (b) (c)

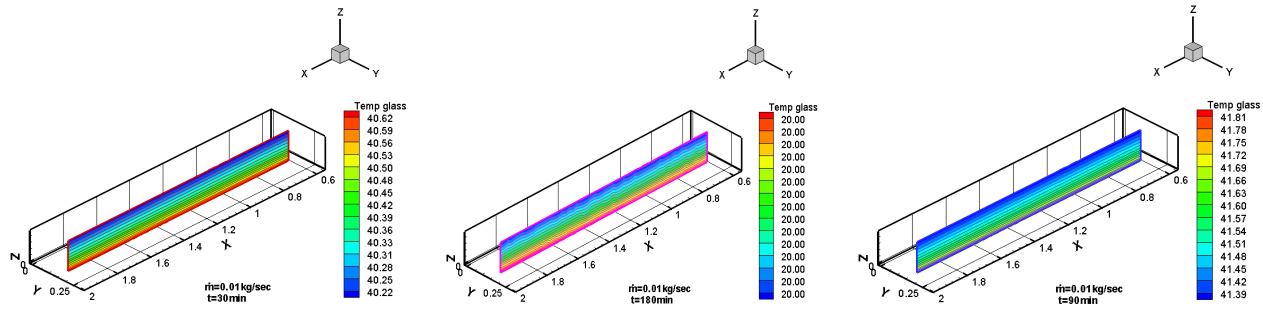
Fig. 8. Air temperature contours along the SAH channel at a mass flow rate of 0.03 kg/s: (a) 30 min, (b) 90 min, and (c) 180 min



(a) (b) (c)

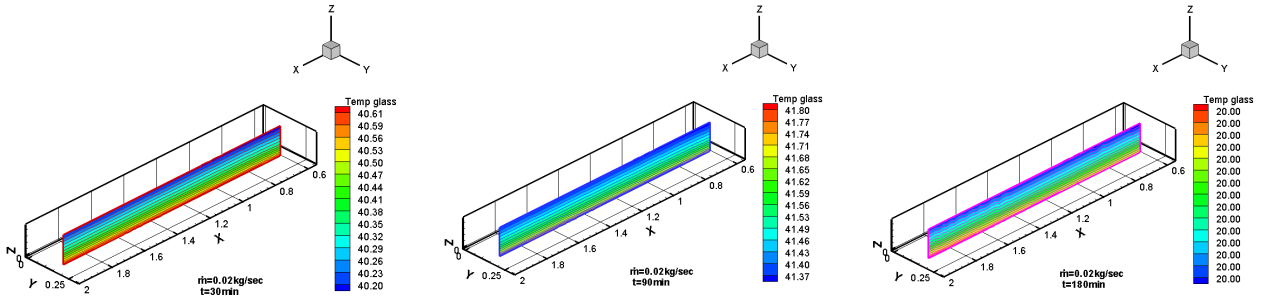
Fig. 9. Air temperature contours along the SAH channel at a mass flow rate of 0.04 kg/s: (a) 30 min, (b) 90 min, and (c) 180 min

Figures 10–13 illustrate the temperature distributions of the glass cover at the four air mass flow rates and elapsed times of 30, 90, and 180 min under a solar irradiance of 502 W/m². The glass cover temperature increased in the streamwise direction along the solar collector.



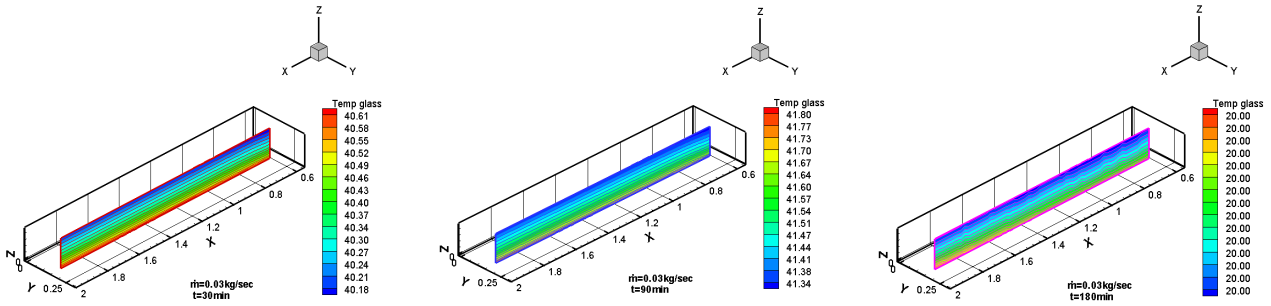
(a) (b) (c)

Fig. 10. Temperature distribution of the SAH glass cover at a mass flow rate of 0.01 kg/s: (a) 30 min, (b) 90 min, and (c) 180 min



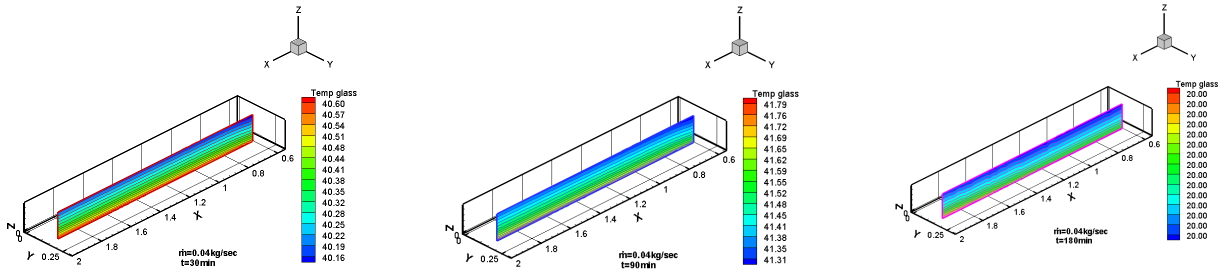
(a) (b) (c)

Fig. 11. Temperature distribution of the SAH glass cover at a mass flow rate of 0.02 kg/s: (a) 30 min, (b) 90 min, and (c) 180 min



(a) (b) (c)

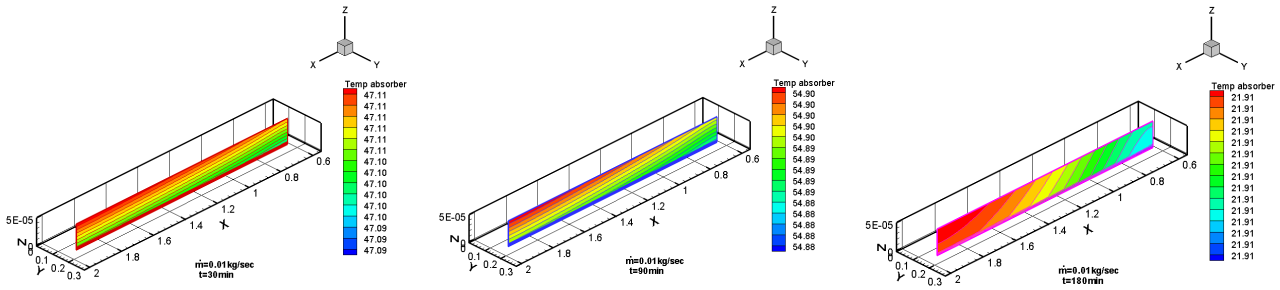
Fig. 12. Temperature distribution of the SAH glass cover at a mass flow rate of 0.03 kg/s: (a) 30 min, (b) 90 min, and (c) 180 min



(a) (b) (c)

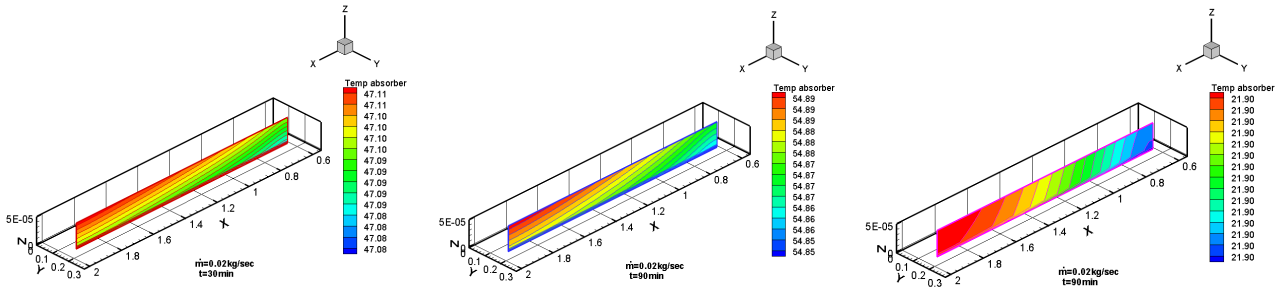
Fig. 13. Temperature distribution of the SAH glass cover at a mass flow rate of 0.04 kg/s: (a) 30 min, (b) 90 min, and (c) 180 min

Figures 14–17 present the temperature distributions of the absorber plate under constant solar irradiance. The absorber plate temperature increased in the streamwise direction and decreased as the inlet air mass flow rate increased. This trend was consistent with enhanced heat removal from the absorber by the flowing air.



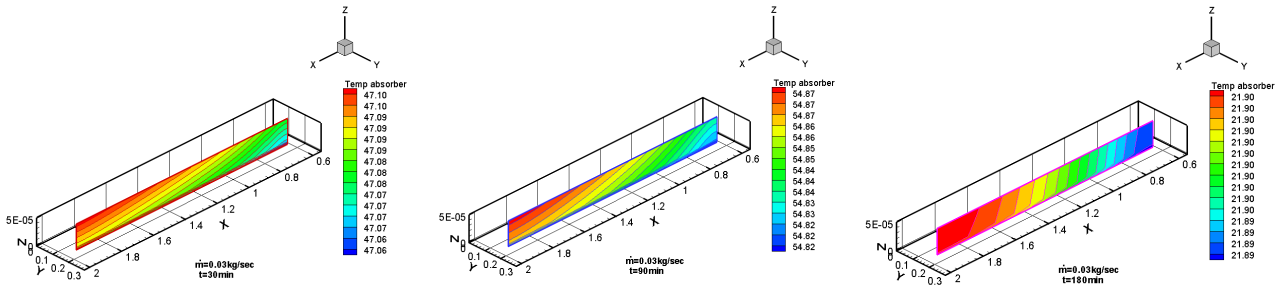
(a) (b) (c)

Fig. 14. Temperature distribution of the absorber plate at a mass flow rate of 0.01 kg/s: (a) 30 min, (b) 90 min, and (c) 180 min



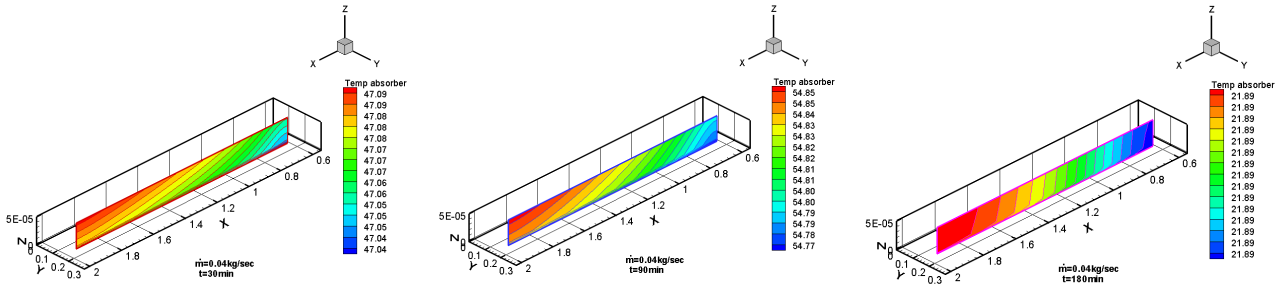
(a) (b) (c)

Fig. 15. Temperature distribution of the absorber plate at a mass flow rate of 0.02 kg/s: (a) 30 min, (b) 90 min, and (c) 180 min



(a) (b) (c)

Fig. 16. Temperature distribution of the absorber plate at a mass flow rate of 0.03 kg/s: (a) 30 min, (b) 90 min, and (c) 180 min



(a) (b) (c)

Fig. 17. Temperature distribution of the absorber plate at a mass flow rate of 0.04 kg/s: (a) 30 min, (b) 90 min, and (c) 180 min

Figure 18 presents the temporal variations in the outlet air, glass cover, and absorber plate temperatures at the four investigated mass flow rates. The glass cover and absorber plate temperatures eventually stabilized, indicating that the system approached thermal equilibrium. Under these conditions, the absorbed solar energy was balanced by heat removal through the airflow and heat losses to the surroundings.

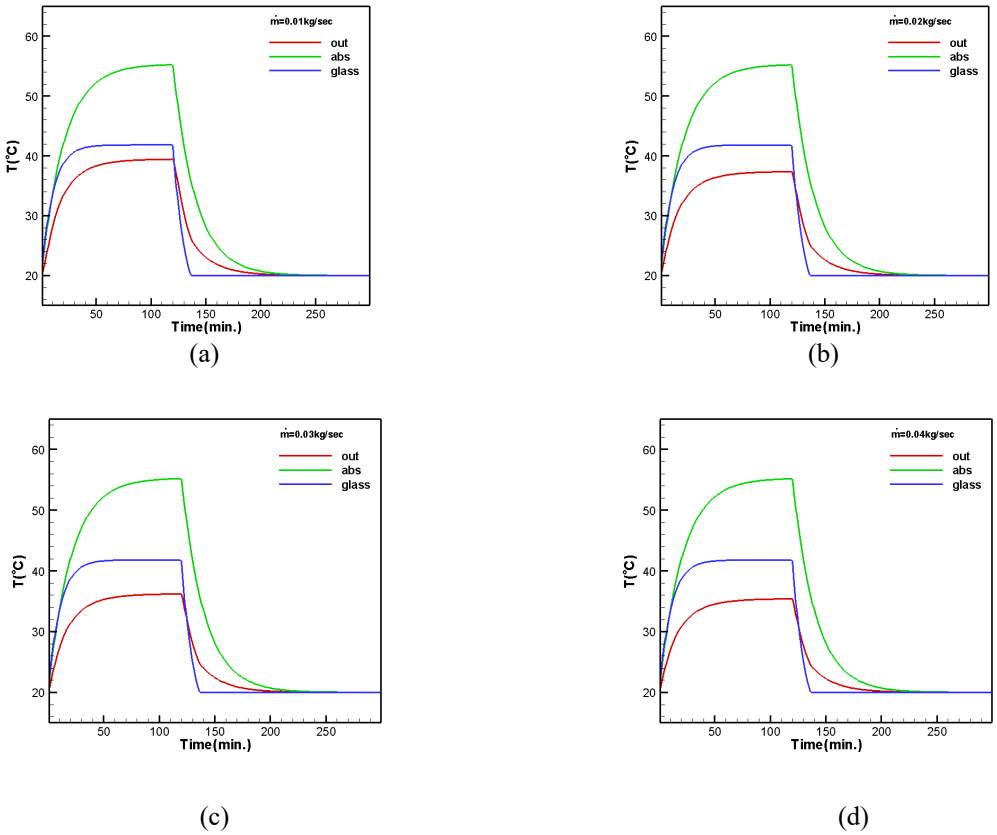


Fig. 18. Temporal variations in outlet air, absorber plate, and glass cover temperatures at mass flow rates of (a) 0.01, (b) 0.02, (c) 0.03, and (d) 0.04 kg/s

Figure 19 illustrates the influence of air mass flow rate on the outlet air temperature. The numerical results revealed that the outlet air temperature increased as the mass flow rate decreased. At lower mass flow rates, a given rate of useful heat transfer produced a greater temperature rise in the airflow. The maximum outlet air temperatures were 40, 38, 36, and 35 °C at mass flow rates of 0.01, 0.02, 0.03, and 0.04 kg/s, respectively.

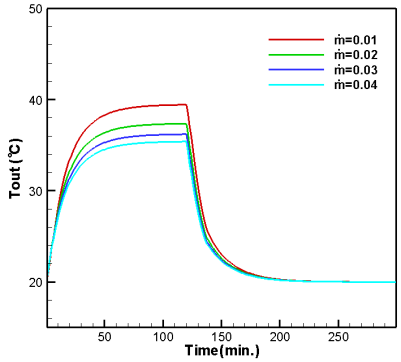


Fig. 19. Outlet air temperature at air mass flow rates of 0.01, 0.02, 0.03, and 0.04 kg/s

Figure 20 illustrates the influence of air mass flow rate on convective heat transfer to the airflow, including the individual contributions of the glass cover and absorber plate. The total convective heat transfer increased with increasing mass flow rate, despite the corresponding reduction in outlet air temperature. These results highlighted the distinction between the temperature rise of the airflow and the total rate of useful heat transfer.

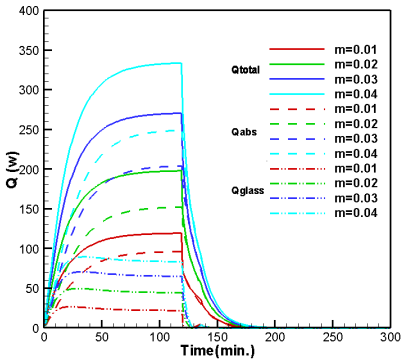


Fig. 20. Convective heat transfer at air mass flow rates of 0.01, 0.02, 0.03, and 0.04 kg/s

As shown in Figure 21, the reported thermal efficiency of the SAH ranged from 20% to 70% over the investigated mass flow rates of 0.01–0.04 kg/s. Thermal efficiency was defined as the ratio of the useful convective heat transfer to the airflow to the total incident solar power on the absorber surface.

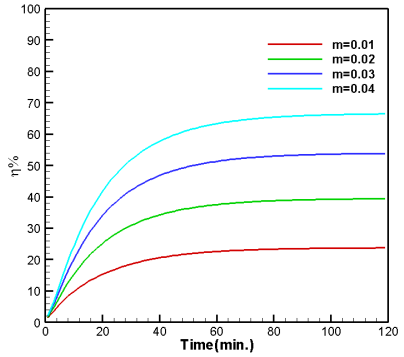


Fig. 21. Thermal efficiency of the SAH at air mass flow rates of 0.01, 0.02, 0.03, and 0.04 kg/s

Figure 22 presents the variation in the Nusselt number with air mass flow rate, including the contributions associated with the absorber plate and glass cover. Convective heat transfer persisted at the absorber surface, whereas the Nusselt number associated with the glass cover was reported to approach zero. The latter result requires further examination because the thermal properties of the glass alone do not establish that convection at its surface was negligible.

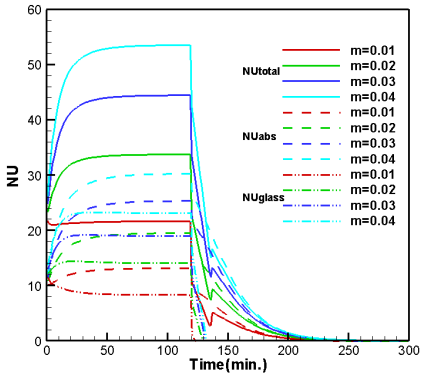
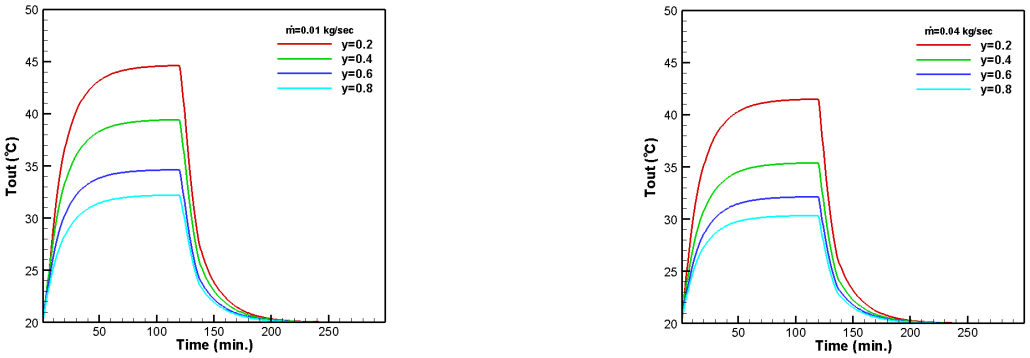


Fig. 22. Nusselt number of the SAH at air mass flow rates of 0.01, 0.02, 0.03, and 0.04 kg/s

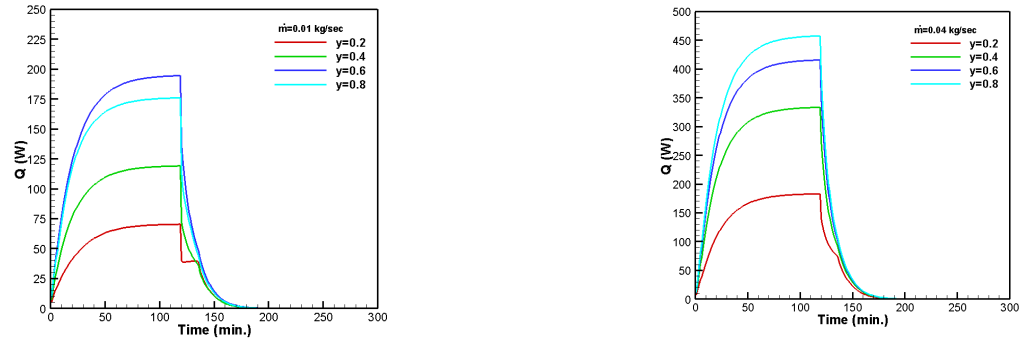
Figure 23 illustrates the effect of air channel height (2, 4, 6, and 8 cm) on outlet air temperature at mass flow rates of 0.01 and 0.04 kg/s. The outlet air temperature increased as the channel height decreased. At a fixed mass flow rate, increasing the channel height increased the flow cross-sectional area and reduced the mean air velocity, potentially altering the convective heat transfer coefficient. Consistent with the earlier results, the lower mass flow rate produced higher outlet air temperatures.



(a) (b)

Fig. 23. Outlet air temperature at channel heights of 2, 4, 6, and 8 cm for mass flow rates of (a) 0.01 and (b) 0.04 kg/s

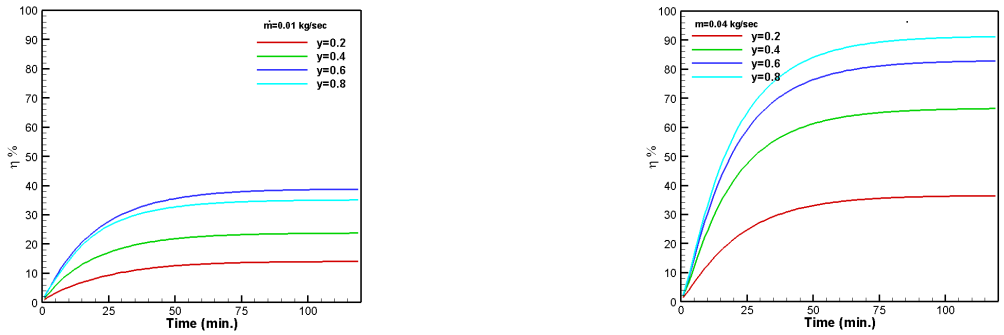
Figure 24 illustrates the effect of channel height on convective heat transfer at mass flow rates of 0.01 and 0.04 kg/s. At 0.01 kg/s, the highest convective heat transfer was obtained at a channel height of 6 cm, whereas at 0.04 kg/s, the highest value was obtained at 8 cm. These results suggested that the optimum channel geometry depended on the operating mass flow rate. Changes in channel height altered the mean velocity, hydraulic diameter, and heat transfer characteristics, although the relative contributions of these mechanisms were not quantified.



(a) (b)

Fig. 24. Convective heat transfer at channel heights of 2, 4, 6, and 8 cm for mass flow rates of (a) 0.01 and (b) 0.04 kg/s

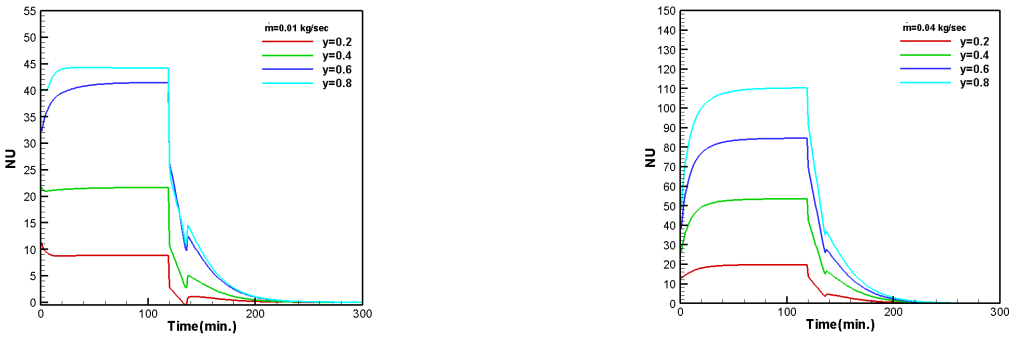
Figure 25 presents the influence of channel height on thermal efficiency. At a mass flow rate of 0.01 kg/s, the maximum efficiency was achieved at a channel height of 6 cm, with lower efficiencies at 2, 4, and 8 cm. At 0.04 kg/s, the maximum efficiency was achieved at a channel height of 8 cm. Among the investigated configurations, the highest overall thermal efficiency was reported at a mass flow rate of 0.04 kg/s and a channel height of 8 cm.



(a) (b)

Fig. 25. Thermal efficiency of the SAH at channel heights of 2, 4, 6, and 8 cm for mass flow rates of (a) 0.01 and (b) 0.04 kg/s

Figure 26 illustrates the variation in the Nusselt number with channel height at mass flow rates of 0.01 and 0.04 kg/s. For both mass flow rates, the maximum Nusselt number was obtained at a channel height of 8 cm. This trend reflected the combined influence of channel geometry and convective heat transfer; however, the effect of hydraulic diameter on the Nusselt number should be distinguished from changes in the heat transfer coefficient.



(a) (b)

Fig. 26. Nusselt number of the SAH at channel heights of 2, 4, 6, and 8 cm for mass flow rates of (a) 0.01 and (b) 0.04 kg/s.

4. Conclusions

A numerical model was developed to investigate the effects of air mass flow rate and channel height on the thermal performance of a single-pass solar air heater. The results indicated that increasing the air mass flow rate enhanced the useful convective heat transfer to the airflow while reducing the outlet air temperature. The optimum channel height for thermal efficiency depended on the operating mass flow rate. Among the investigated channel heights, the maximum thermal efficiency was obtained at 6 cm for a mass flow rate of 0.01 kg/s and at 8 cm for a mass flow rate of 0.04 kg/s. The latter configuration yielded the highest reported thermal efficiency among the investigated combinations.

The findings provided useful insights for the design and optimization of solar air heaters for air heating and agricultural drying applications. Further investigations should examine a wider range of channel geometries and operating conditions, quantify model prediction errors, and evaluate

pressure losses alongside thermal performance to establish the practical applicability of the proposed model.

Acknowledgement
This research received no grant funding.

Reference

[1] Korti, Abdel Illah Nabil. "Numerical 3-D Heat Flow Simulations on Double-Pass Solar Collector with and without Porous Media." *Journal of Thermal Engineering* 1 (2015): 10–23.
[2] Panda, Sudharani, and Rakesh Kumar. "A Review on Heat Transfer Enhancement of Solar Air Heater Using Various Artificial Roughed Geometries." *Journal of Advanced Research in Fluid Mechanics and Thermal Sciences* 89, no. 1 (2022): 92–133.
[3] Dheyab, Hussam, Manar Salih, Manar Al-Jethelah, Tadahmun Yassen, and Thamir Khalil. "Experimental Study of the Optimum Air Gap of a Rectangular Solar Air Heater." *Journal of Advanced Research in Fluid Mechanics and Thermal Sciences* 59, no. 2 (2019): 318–329.
[4] Saberi, Zainab, Ahmad Fudholi, Noorlina Mohd Zainuddin, Zahari Ibarahim, and Kamaruzzaman Sopian. "Thermal Performance of an Absorber Rod Type Solar Air Collector with Single-Path Design." *Journal of Advanced Research in Fluid Mechanics and Thermal Sciences* 69 (2020): 1–12.
[5] Halassa, Daoud, Mohamed Announ, Abdelghani Boubekri, Djamel Mennouche, and Hamza Bouguettaia. "Thermal Performance Analysis of a Solar Air Heater with Different Baffle Configuration." *Journal of Advanced Research in Fluid Mechanics and Thermal Sciences* 61, no. 2 (2019): 233–247.
[6] Sheshadri, Arunkumar Honnesara, Madhwesh Nagaraja, Anirudh Hegde K., Manjunath Mallashetty Shivamallaiah, Kota Vasudeva Karanth, and Younes Amini. "Effect of Chamfered Turbulators on Performance of Solar Air Heater—Numerical Study." *CFD Letters* 16, no. 11 (2024): 17–36.
[7] Mushatet, Khudheyer S., and Rawan A. Fayyad. "Experimental Investigation for Performance Evaluation of Solar Air Heater Collector." *AIP Conference Proceedings* 2398 (2022): 020042.
[8] Abdullah, Yussra Malallah, Ghadeer Salim Aziz, Hala Kaydar Salah, and Hussein Kadhim Sharaf. "Simulate the Rheological Behaviour of the Solar Collector by Using Computational Fluid Dynamic Approach." *CFD Letters* 15, no. 9 (2023): 175–182.
[9] Rasheed, Maithum Hussein. "Performance Enhancement of Solar Air Heater Using Different Phase Change Materials (PCMs)." *Journal of Advanced Research in Fluid Mechanics and Thermal Sciences* 66, no. 1 (2020): 64–75.
[10] Srivastava, Mayank, G. Phal Dessai, Divya Srivastava, Pardeep Bishnoi, Pravin Singh, and M. K. Sinha. "Thermal Analysis of Solar Air Heater by Using Pebbles as an Absorber Material." *AIP Conference Proceedings* 2341 (2021): 030018.
[11] Le, Minh Nhut, Ha Nguyen Minh, and Luan Nguyen Thanh. "The Effective and Exergy Efficiency of Multi-Pass Solar Air Collector with Longitudinal Fins: Analysis and Optimization." *Journal of Advanced Research in Fluid Mechanics and Thermal Sciences* 102, no. 2 (2023): 42–65.
[12] Harun, Muhammad Amin, Zafri Azran Abdul Majid, Zairul Azrul Zakaria, Ahmad Faris Ismail, Sany Izan Ihsan, Kamaruzzaman Sopian, Ahmad Fadzil Sharol, and Amir Abdul Razak. "Study on Selection of a Suitable Material and the Parameters for Designing a Portable Flat Plate Base-Thermal Cell Absorber (FPBTCA)." *Journal of Advanced Research in Fluid Mechanics and Thermal Sciences* 85, no. 1 (2021): 71–92.
[13] Hardan, Abdulwahhab A., Israa S. Ahmed, and Mohammed J. Mohammed. "Experimental Investigation of the Performance of Evacuated Tube Solar Collector with Finned Heat Pipe." *AIP Conference Proceedings* 3002 (2024): 070007.
[14] American Society of Heating, Refrigerating and Air-Conditioning Engineers (ASHRAE). *Methods of Testing to Determine the Thermal Performance of Solar Collectors*. ASHRAE Standard 93-77. New York: ASHRAE, 1977.
[15] Patankar, Suhas V. *Numerical Heat Transfer and Fluid Flow*. Hemisphere Publishing Corporation, 1980.
[16] Incropera, Frank P., and David P. DeWitt. *Fundamentals of Heat and Mass Transfer*. 5th ed. John Wiley & Sons, 2002.
[17] Prakash, Mahesh, Ozden Turan, and Graham Thorpe. "Program NATCON: For the Numerical Solution of Buoyancy-Driven Laminar and Turbulent Flows in Differentially Heated Cavities." 2006.
[18] Doan, Thi Hong Hai, and Nguyen Minh Phu. "A Critical Review of All Mathematical Models Developed for Solar Air Heater Analysis." *Journal of Advanced Research in Fluid Mechanics and Thermal Sciences* 105, no. 1 (2023): 1–14.

[19] Bergman, Theodore L., Frank P. Incropera, David P. DeWitt, and Adrienne S. Lavine. *Fundamentals of Heat and Mass Transfer*. 7th ed. John Wiley & Sons, 2011.
[20] Baredar, Prashant V., Srinivas Tangellapalli, and Chetan Singh Solanki, eds. *Advances in Clean Energy Technologies*. 2020.